Title

Effective mechanical potential of cell–cell interaction in tissues harboring cavity and in cell sheet toward morphogenesis

Short title

Effective potential of cell–cell interaction in 2D and 3D

Authors

Hiroshi Koyama[1,2,*], Hisashi Okumura[2,3,4], Tetsuhisa Otani[2,5], Atsushi M. Ito[6], Kazuyuki Nakamura[7,8], Kagayaki Kato[2,9], and Toshihiko Fujimori[1,2]

[1]Division of Embryology, National Institute for Basic Biology, 5-1 Higashiyama, Myodaiji, Okazaki, Aichi 444-8787, Japan

[2]SOKENDAI (The Graduate University for Advanced Studies), 5-1 Higashiyama, Myodaiji, Okazaki, Aichi 444-8787, Japan

[3]Biomolecular Dynamics Simulation Group, Exploratory Research Center on Life and Living Systems (ExCELLS), National Institutes of Natural Sciences, 5-1 Higashiyama, Myodaiji, Okazaki, Aichi 444-8787, Japan

[4]Institute for Molecular Science, National Institutes of Natural Sciences, 5-1 Higashiyama, Myodaiji, Okazaki, Aichi 444-8787, Japan

[5]Division of Cell Structure, National Institute for Physiological Sciences, 5-1 Higashiyama, Myodaiji, Okazaki, Aichi 444-8787, Japan

[6]National Institute for Fusion Science, National Institutes of Natural Sciences, 322-6 Oroshi-cho, Toki, Gifu 509-5292, Japan

[7]School of Interdisciplinary Mathematical Sciences, Meiji University, 4-21-1 Nakano, Nakano-ku, Tokyo 164-8525, Japan

[8]JST, PRESTO, 4-1-8 Honcho, Kawaguchi, Saitama 332-0012, Japan

[9]Optics and Imaging Facility, Trans-Scale Biology Center, National Institute for Basic Biology, 38 Nishigonaka, Myodaiji, Okazaki, Aichi 444-8585, Japan

*Correspondence: Hiroshi Koyama

Division of Embryology, National Institute for Basic Biology, 5-1 Higashiyama, Myodaiji, Okazaki, Aichi 444-8787, Japan

Phone: +81 564 59 5862,

hkoyama@nibb.ac.jp.

Conflicts of interest

The authors declare no competing financial interests.

Keywords

effective potential of cell–cell interaction, morphological diversity, mechanics, emergent property of multicellular system, mouse blastocyst, MDCK cyst

This file includes:

- Main text
- Figure 1 to 8

Abstract

Measurement of mechanical forces of cell–cell interactions is important for studying the emergence of diverse three-dimensional morphologies of multicellular organisms. We previously reported an image-based statistical method for inferring the effective mechanical potentials of pairwise cell–cell interactions, where cell tracking data obtained by live imaging was fitted by a theoretical model. However, because real tissues harbor various non-cellular components such as expanding cavities, whether the image-based method is applicable to such tissue remains elusive. Here we evaluated the applicability of the method in cavity-harboring tissues. First, we used synthetic data generated by simulations under cavities with pregiven cell–cell interaction potentials, to which our inference method was applied. The inferred effective potentials showed a profile modified from the pregiven potentials, but subsequent analyses revealed that the pregiven potentials can be reconstructed by substituting the effect of the expanding cavities which emerged as an additional repulsive component around long-distance of cell–cell interactions. Interestingly, simulations by using the modified effective potentials reproduced the cavity-harboring structures, implying that the effect of expanding cavities was approximately incorporated into the effective pairwise potentials. Then, we applied our inference method to the mouse blastocyst and cysts of Madin-Darby canine kidney

(MDCK) cells, and found that the inferred effective potentials can reproduce the cavity-harboring structures. A similar modification of pairwise potentials was also detected in two-dimensional cell sheets, by which curved sheets such as tubes and cups were simulated. We conclude that our inference method is applicable to tissues harboring cavities and cell sheets, and the resultant effective potentials are useful to simulate the morphologies.

Introduction

In multicellular living systems, various three-dimensional morphologies are emerged, which is thought to be primarily dependent on the mechanical properties of the constituent cells (Bazellières et al., 2015; Fletcher et al., 2014; Guillot and Lecuit, 2013; Maître et al., 2012; Steinberg, 2007). Measurement of cellular mechanical parameters is inevitable for understanding morphogenetic events. On the other hand, morphogenetic events are also influenced by non-cellular structures such as cavities, extracellular matrix, etc (Style et al., 2014; Wang et al., 2018). Therefore, it is challenging to identify all components contributing to morphogenetic events, and then, to measure their mechanical forces especially under three-dimensional situations.

Image-based methods for inferring mechanical forces in tissues have been developed, where mathematical models are assumed which are fitted to microscopic images (Brodland et al., 2010; Ishihara and Sugimura, 2012; Kondo et al., 2018; Koyama et al., 2023, 2012; Merkel and Manning, 2017; Miyoshi et al., 2006). These methods include inference of cell–cell junction tensions in two-dimensional epithelia, cell surface tensions or bending rigidities, mechanical potential of pairwise cell–cell interactions, etc. Basically, these methods do not assume non-cellular structures in their mathematical models, and, it is unknown whether these methods are applicable to tissues with non-

cellular components.

We previously reported a method for inferring mechanical potential of pairwise cell–cell interactions (Koyama et al., 2023). The pairwise potentials are composed of attractive and repulsive forces of cell–cell interactions. The attractive forces are at least partially derived from cell–cell adhesion forces mediated by cell adhesion molecules (Fig. 1A-B), whereas the repulsive forces are from excluded volume effect of cells (Drasdo et al., 1995; Forgacs and Newman, 2005; Guillot and Lecuit, 2013; Maître et al., 2012; Merkel and Manning, 2017; Steinberg, 2007; Yong et al., 2015). The summation of these forces would be dependent on cell–cell distance (Fig. 1C), by which the pairwise potential energy is calculated. We previously showed that, by applying our method to the mouse and *C. elegans* early embryos which did not still harbor clear cavities or thick extracellular matrix, we obtained mechanical potential of pairwise interactions (Koyama et al., 2023). The profiles of the pairwise potentials were quantitatively different among the tissues, by which the morphologic features of the corresponding tissues were reproduced.

In the present study, we evaluated whether our inference method is applicable to cavity-harboring tissues such as the mouse blastocysts (Fig. 1D). First, we theoretically analyzed the effect of liquid cavities by using synthetic data which were generated by simulations under pregiven cell–cell forces and cavities. In the case where the cavities are

expanding, the inferred effective pairwise forces of cell–cell interactions became significantly different from the pregiven forces, where an additional repulsive component was detected. But we showed that the repulsive component was derived from the expanding cavities, and that the inferred effective pairwise forces were the summation of both the pregiven forces and the effect of the expanding cavities. Therefore, simulations using inferred pairwise forces successfully reproduced the cavity-harboring structures. Application of our method to the mouse blastocyst and the cysts of MDCK cells also resulted in the same conclusion. Finally, we systematically analyzed what kind of profiles of the effective pairwise potentials are critical for forming cavity-harboring structures, which were presented as phase diagrams, and expanded the analyses to curved sheets.

Results

Inference of effective pairwise potential in synthetic data with cavity

In our inference method, a cell-particle model is assumed where attractive/repulsive forces of cell–cell interaction is considered (Fig. 1B-C), and the mathematical model is fitted to nuclear tracking data (i.e., *xyz*-coordinates of each nucleus with the time series) as described previously (Koyama et al., 2023). Briefly, the fitting procedure is based on a minimization of the differences between the *xyz*-coordinates of particles in the mathematical model and in the nuclear tracking data, with an additional cost function for cell–cell distance-dependent weight. The fitting parameters are the force values for each pair of two interacting cells for each time frame, and then, by binned averaging the inferred forces along cell–cell distances, a distance–force curve is calculated. In the model to be fitted, we do not explicitly consider non-cellular structures exerting forces on cells. It can be argued that, if tissues harbor non-cellular structures, the model should assume the non-cellular structures. But, due to high degrees of freedom in such models, the fitting problems would become difficult to be solved in general. We intended to analyze whether valuable information can be obtained when our inference method is applied to tissues with cavities (Fig. 1D). To this aim, we first generated simulation data considering both cell–cell interaction forces and cavities, to which we

applied our inference method.

In our simulations based on particulate cells, the cell–cell interaction forces were set to be provided by the Lenard-Jones (LJ) potential (i.e., the pregiven forces) in a similar manner to our previous work (Koyama et al., 2023), and expanding cavities was also provided. In real tissues, cavities are generated by secreting liquid from cells. The cell layers surrounding the cavities are sealed by the tight junctions, and thus the pressure of the cavities push the cells outward (Fig. 1D) (Dumortier et al., 2019; Moriwaki et al., 2007; Wang et al., 2018). In simulations, we implemented expanding spherical cavities as temporally-evolved spatial constraints; the particulate cells cannot penetrate into the cavities (Fig. S1A-B and movieS1), leading to that the particles move on the surfaces of the cavities.

Fig. 2A-I shows the snapshot of the simulations where the spherical cavity was expanding from the radius = 9.6 to 12.6μm. Fig. 2A-ii shows inferred effective distance–force (DF) curves under three different conditions of the expanding cavities; the inferred DF curves were not consistent with the DF curves from the LJ potential (Fig. 2A-ii, compare with the black broken line), where repulsive components were strongly detected especially at distant regions, which we call distant energy barrier (DEB). The strength of the repulsive components seemed to be positively related to the expansion rates. In

contrast, under the conditions of non-expanding cavities, the inferred DF curves were consistent with the LJ potential (Fig. S1C).

We then examined whether this modification is meaningless or is a result of a correct reflection of the expanding cavities. By performing simulations under conditions with the expanding cavities but without the LJ potential (i.e., without cell–cell interaction forces) (Fig. 2B-i), we solely extracted the influence of the expanding cavities. Fig. 2B-ii shows that the inferred effective DF curves were absolutely composed of repulsive components. Then, we checked the raw data where all data points were plotted on the distance–force space; in Fig. 2C-i, "From B", a heat map of the data points is shown. Force values calculated by binned averaging are also shown in yellow, which correspond to the DF curve in Fig. 2B-ii (red line). Interestingly, all the data points were closely located around the DF curve ("From B"), implying that the DF curve is a good approximation of the expanding cavities. Probably, due to the effect of the expanding cavities which causes the increases in distances among the particles, pairwise forces of particle–particle interactions became apparently repulsive.

Finally, by using the above information, we examined whether the correct DF curve (i.e., LJ potential) can be reconstructed. We subtracted the DF curves in Fig. 2B from those in Fig. 2A (Fig. 2C-i, "From A – From B"), and the resultant DF curves were

182 well consistent with the LJ potential under any expansion rates of the cavities (Fig. 2C-
183 ii). These results suggest that the effects of the expanding cavities can be addible to
184 effective DF curves.

185 We interpret the above results as described in Fig. 2D. A cell receives forces from
186 cell–cell interactions ("LJ" in Fig. 2D) and from the pressure of the cavity, where the
187 vector of the pressure is perpendicular to the surface of the cavity (Fig. 2D, top panel).
188 The repulsive forces detected as cell–cell interactions in Fig. 2A are described in Fig. 2D,
189 middle panel (light blue vectors), and the vector of the net force (a red vector) for a cell
190 is perpendicular to the surface of the cavity, if the cells are almost uniformly distributed.
191 Therefore, the pressure from the cavity can be equivalent to the net force from the DEBs
192 (Fig. 2D, bottom panel), leading to the successful reconstruction of the LJ potential.

193 We conclude that the expanding cavities can be approximated as effective
194 pairwise potentials. In general, effective pairwise forces/potentials are the summation of
195 different components as explained in Fig. 1C. External factors are one of the components
196 to be summed up in molecular and colloidal sciences: e.g., by considering hydration of
197 particles by solvents, effective pairwise potentials are modified so as to contain energy
198 barriers around distant regions (Israelachvili, 2011; Pettitt and Rossky, 1986), and such
199 effective potentials have been used to simulate behaviors of the systems. We will show

200 the simulation outcome from the above inferred effective DF curve later.

201

202 *Effective forces in mouse blastocyst contained DEB*

203 To investigate whether a repulsive component appeared in effective forces
204 inferred from the mouse blastocyst (Fig. 3A, illustration). An inner cavity is formed
205 through liquid secretion from the cells, and the embryos expand while maintaining their
206 spherical shape (Dumortier et al., 2019; Moriwaki et al., 2007; Wang et al., 2018) (Fig.
207 3A, bright field and cross-section). Trophectoderm (TE) cells form a single-cell-layered
208 structure at the outermost surface of the embryo, whereas the cells of the inner cell mass
209 (ICM) were tightly assembled, forming a cluster (Fig. 3A, illustration). We performed
210 cell tracking (Fig. 3A, tracking) and inferred effective forces.

211 Fig. 3B shows the inferred effective DF curve from the blastocyst. The DF curve
212 contained the repulsive component around distant regions (Fig. 3B, DEB). For
213 comparison, an inferred DF curve from an embryo before forming a cavity is shown,
214 which did not contain DEB (Fig. 3B, "compaction" meaning the embryo at the
215 compaction stage). In addition, Fig. 3C shows the distance–potential (DP) curves which
216 can be calculated from the DF curves, and the DEB appeared as a long slope.

217 To further examine whether the DEB was derived from the cavity, we inhibited

218 the cavitation by using an inhibitor for Na^+/H^+ exchanger (S3226) (Kawagishi et al.,
219 2004). Fig. 3D shows the inhibitor-treated embryos; the experimental procedures are
220 shown in Fig. S2. Fig. 3D shows the inferred effective DP curves, where DEB was
221 diminished, indicating that the cavity yielded the DEBs.
222
223 *Effective forces in MDCK cyst contained DEB*
224 We also applied our method to other tissues harboring cavities. MDCK cells can
225 form cysts containing a cavity when cultured under suspension conditions (Fig. 4A)
226 (Wang et al., 1990). Fig. 4B and 4C show the effective DF and DP curves, where a DEB
227 was detected.
228
229 *Effective potentials reproduced cavity-harboring structures*
230 Effective DF/DP curves are the summation of the multiple components including
231 the excluded volume effect, adhesive forces, and external factors, and are useful to study
232 behaviors of systems in molecular and colloidal sciences. We evaluated whether inferred
233 effective DF/DP curves from the cavity-harboring systems can reproduce their
234 morphologies. The effective DF curves inferred from the mouse blastocyst, the MDCK
235 cyst, and the artificial tissue harboring a cavity (Fig. 2-4) were used for simulations, and

236 the systems were relaxed to find stable states. When initial configurations of particles
237 were set to be cavity-harboring structures (Fig. 5A), the structures were maintained (Fig.
238 5B-D, left panels). To examine whether the DEBs contribute to the formation of the
239 cavities, we artificially eliminated the DEBs from the DF curves, and performed
240 simulations. We found that cavities were not maintained but aggregates — filled with the
241 particles — were formed (Fig. 5B-C, "DF curve w/o DEB"). For comparison, we used
242 the Lenard-Jones potential, and showed that the cavity-harboring structure was not
243 maintained but became an aggregate (Fig. 5E).
244
245 *Modeling of distance–force curves with two parameters*
246 To comprehensively understand the effect of the differences of the profiles in
247 the DF curves on morphogenesis, we modeled the DF curves as a simple mathematical
248 equation. To analyze the contribution of DEBs, we selected the following equation (Fig.
249 6A, left panel, blue line):
250 $$F(D) = \varepsilon(D - D_0)^{-N} \cos\left\{\frac{2\pi(D - D_0)}{\delta}\right\}, \text{ for } D > D_0 \qquad \text{(Eq. 1)}$$
251 Here, F is the force, D is the distance. N is the exponent of D, affecting the decay of the
252 DF curves along D (X-axis) (Fig. 6A, left panel, green broken line). To model DEB, we
253 introduced a cosine function whose wavelength is affected by δ; the combination of the

254 above exponential function (Fig. 6A, left panel, green broken line) with the cosine
255 function (Fig. 6A, left panel, purple broken line) resulted in a function bearing DEB (Fig.
256 6A, left panel, red line). D_0 can translate the DF curves along D, (Fig. 6A, left panel, red
257 vs. blue lines). This translation simultaneously modifies the relative positions of DEBs to
258 the mean diameters (Fig. 6A, left panel, where D_1, mean diameter; D_2, distance at DEB;
259 $D_3 = D_2/ D_1$, the relative positions of DEB). N also affects the strengths of DEBs (Fig.
260 6A, right panel, F_{rep}/F_{att} is the relative strength of DEB).

261 All parameters and variables related to lengths/distances were normalized by
262 (δ/4), leading to generation of dimensionless parameters and variables such as $D_0^* = D_0$
263 /(δ/4). In addition, ε does not contribute to morphologies under stable states. Therefore,
264 we can present simulation outcomes in two-dimensional space (D_0^* and N) in a manner
265 similar to a phase diagram (Fig. 6B) as shown in the next section. Although there can be
266 other equations modeling DF curves, the advantage of this equation is that it is composed
267 of just two parameters (D_0^* and N).

268

269 *Appropriate position and strength of DEB were essential for cavity-harboring structures*

270 First, we examined what kind of DF curves can maintain a cavity-harboring
271 structures. In simulations of multicellular systems, the morphologies are determined by

both DF curves and initial configurations, because energetic local minimum states (i.e. metastable state) as well as global minimum states are meaningful. A cavity-harboring structure was set as the initial configuration (Fig. 6B, "Initial configuration"), and simulations were performed until the systems reached steady states including metastable states.

Fig. 6B shows a phase diagram with representative images of the simulations, on which two regions of cavity-harboring structures were identified ("cavity" and "cavity with extra particles"). The "cavity" class absolutely depended on the DEBs, because DF curves whose DEBs were eliminated did not form the "cavity" as shown in Fig. 6C ("w/o DEB"). We confirmed that the cavity was not broken by slight positional fluctuations (Movie S2), indicating that the structures were stable. In Fig. 6B, the "cavity" class was located around smaller N values (less than ~2.0), otherwise the "aggregate" class was formed, suggesting that the strengths of the DEBs, defined in Fig. 6A (right panel), may be effective. Furthermore, larger D_0 values were required for the "cavity" class, otherwise the "multiple clusters/disorganized" class was formed, suggesting that the relative positions of DEBs ($D_3 = D_2/ D_1$ in Fig. 6A, left panel) should be close to the mean diameters. In addition, the "cups" and "tubes" classes were found between the "cavity" and the "multiple clusters/disorganized" classes in Fig. 6B but not in Fig. 6C, indicating

290 that the DEBs also contribute to the formation of these structures. Under a different
291 number of particles, a similar trend was observed (Fig. S4). The maintenance of tubes
292 was confirmed to be dependent on DEBs (Fig. S5).
293
294 *Profiles of DF curves for describing 2D sheet*
295 To further investigate the capability of DF curves, we next applied a two-
296 dimensional (2D) sheet as the initial configuration which corresponds to a monolayered
297 cell sheet (Fig. 7A, "Initial configuration"). Fig. 7A shows a phase diagram with
298 representative simulation images. The 2D sheets were maintained (the "sheet" class),
299 which was largely dependent on the presence of DEBs (Fig. 6A, w/ DEBs vs. 6B, w/o
300 DEBs). We confirmed that the 2D sheets were not broken by slight positional fluctuations
301 (Movie S2), indicating that the structures were stable. The region of the "sheet" class was
302 located around larger values of D_0, which was a similar trend to the case of the cavity in
303 Fig. 6. In addition, the cavity-harboring structures were newly generated even in the
304 absence of the DEBs (Fig. 7B). By temporally changing N, D_0, and existence of DEB, we
305 presented possible morphological transitions among the classes in Fig. 6 and 7 (Fig. S6
306 and movie S3).
307

Profiles of DF curves for describing spherical/non-spherical aggregates

In Fig. 7, we found that both the "spherical" and "non-spherical aggregate" classes were generated w/ and w/o DEBs. Smaller values of N and/or D_0 led to the spherical ones (Fig. 7B). Under smaller values of D_0, because the width (W_1 ; see the bottom row in Fig. 7) of the attractive force regions in DF curves became relatively long compared to the mean diameter (D_1, in Fig. 7), the resultant increased attractive forces may cause the spherical aggregates. Under smaller values of N, the potential energies (P_1, in Fig. 7) derived from the attractive forces are increased, possibly leading to the spherical aggregates.

Effective forces in 2D sheets included DEB

As shown in Fig. 7, 2D sheets were maintained under the DF curves including DEB. Similarly, the cups and tubes in Fig. 6 were also maintained under the DF curves including DEBs; these structures can be interpreted as a curved sheet. Is the relationship between these structures and DEB an artifact or are there any reasonable explanations?

To investigate this issue, we used synthetic 2D sheets generated by simulations (Fig. 8A-i). The 2D simulations were performed under the Lenard-Jones (LJ) potential as the pregiven force, and the DF curves were inferred. As shown in Fig. 8A-i, the inferred

326 DF curve was similar to the LJ potential, but the curve contained a clear DEB. This was
327 contrast to the inferred DF curve from the simulation of a 3D aggregate, where DEB was
328 rarely detected (Fig. 8A-ii).

329 We hypothesized that the radial distribution functions (RDF) between 2D and
330 3D situations were different, because RDFs are related to the profile of distance–potential
331 curves in atomic/molecular/colloidal sciences (Israelachvili, 2011). RDFs mean the
332 density of particles at a certain distance from a particle of interest (Fig. 8B). The density
333 may be reflected as the effective potential energy at the distance; high density corresponds
334 to low potential energy (Fig. 8B). In other words, by using RDFs, effective pairwise
335 potentials are calculated if the systems are under equilibrium conditions.

336 We calculated RDFs in 2D and 3D simulations performed under the LJ potential
337 (Fig. 8C). In these simulations, fluctuations of the forces of cell–cell interactions were
338 assumed with the persistency of the fluctuations (the details are described in
339 Supplementary information). Under the 2D situations, clear peaks were found where the
340 particle density was high. Importantly, between the peaks, the density was very low (Fig.
341 8C-i, black arrow). By contrast, under the 3D simulations, relatively unclear peaks were
342 detected, and the regions with low particle densities almost disappeared (Fig. 8C-ii).
343 Additionally, even under the 2D simulations, the longer persistency caused disappearance

of the regions with low particle densities, because the long persistency promotes the movements of the particles. These results suggest that 2D sheets spontaneously yield regions with low particle density in RDF, probably due to the geometric reasons, and that this feature can be reflected to the effective pairwise potentials as DEB.

Discussion

In this study, by inferring effective forces of cell–cell interactions in tissues harboring expanding cavities, we showed that the effect of the cavities was addible to the effective forces of cell–cell interactions as a repulsive component (DEB). The resultant distance–force curves reproduced the tissue structures harboring cavities in simulations. A similar repulsive component was also detected in two-dimension (2D) cell sheets, which may be derived from geometric reasons of 2D systems. Finally, by assuming distance–force curves with the repulsive components, tissue structures of 2D sheets, cups, and tubes were reproduced in simulations. These results suggest that external components and geometric constraints can be correctly added to the effective forces of cell–cell interactions. This framework considering the repulsive components can be useful to simulate and study morphogenesis of 2D sheets and their derivatives (i.e., cavity-harboring structures, cups, and tubes as curved sheets) (Belmonte et al., 2016; Eiraku et

al., 2011; Honda et al., 2008b; Koyama et al., 2016; Montesano et al., 1991; Rivron et al., 2018; Serra et al., 2019; Solnica-krezel and Sepich, 2012; Wang et al., 1990).

Influence of external factors on effective potentials

Our results suggest that expanding cavities and geometric features of 2D sheet can be incorporated into the effective pairwise potentials. In atomic/molecular/colloidal sciences, it is known that some external factors are addible to effective pairwise potentials. For instance, particles such as ions and colloids are hydrated by water molecules as solvents, resulting in that the effective pairwise potentials of the particles contain repulsive components at distant regions, and the resultant potentials explain the behaviors of the systems (Israelachvili, 2011). External pressures can modify RDF by increasing density of the particles, leading to the modification of the effective pairwise potentials. In multicellular systems, it is unknown what kind of external factors are addible to the effective pairwise potentials. We speculate that, if external factors uniformly exert forces on cells, the effect may be correctly incorporated into the effective potentials.

Comparison of other inference methods with other models

To understand morphogenetic events, simulations based on mechanical

380 parameters are essential. Models such as vertex, Cellular Potts, and phase field models
381 are often utilized, especially for epithelial cells (Belmonte et al., 2016; Camley et al.,
382 2014; Fletcher et al., 2014; Honda et al., 2008a; Nonomura, 2012). These models
383 successfully recapitulated various morphogenetic events, including the formation of the
384 mouse blastocyst (Honda et al., 2008a). However, it is still challenging to measure cellular
385 and non-cellular parameters in three-dimensional systems with high spatiotemporal
386 resolution. Image-based force inference methods are important techniques (Ishihara and
387 Sugimura, 2012; Tambe et al., 2011). However, in the case that tissues harbor non-cellular
388 factors, it becomes difficult to infer due to increased degrees of freedom. Our idea can
389 reduce the degrees of freedom, and may be adapted to other image-based inference
390 methods when non-cellular factors exist. Our goal is to develop a framework for
391 explaining diverse morphogenesis in a minimal model. Approximations of some external
392 factors as effective potentials of cell–cell interaction serve to reduce degrees of freedom.
393

394 Materials and methods

395 **Mouse embryos**

396 Embryos were obtained after mating homozygous R26-H2B-EGFP knock-in male
397 mice which constitutively express EGFP (enhanced green fluorescent protein)-fused H2B

398 (histone2B proteins) (Kurotaki et al., 2007) and ICR female mice (Japan SLC). The
399 embryos were cultured in EmbryoMax KSOM +AA with D-Glucose (Millipore, USA)
400 covered with mineral oil on a glass bottom dish (35-mm; 27-mm ϕ, Matsunami, Japan) at
401 37°C, and subjected to microscopic imaging. Four distinct embryos were analyzed.

402 In the experiments using S3226 (Fig. S9), the E2.5 embryos were transferred to the
403 medium with the drug. After 15 hours culture, some embryos failed to form cavities (Fig.
404 S9, #1 and #2), while others formed smaller cavities (Fig. S9, #3) than that under no-drug
405 conditions (Fig. S9, No drugs). Live imaging was performed, and then a rescue process
406 was carried out, resulting in that the embryos formed, at least, smaller cavities compared
407 with that under no-drug conditions. The concentration of S3226 was 50μM.

408 Animal care and experiments were conducted in accordance with National Institutes
409 of Natural Sciences (NINS), the Guidelines of Animal Experimentation. The animal
410 experiments were approved by The Institutional Animal Care and Use Committee of
411 NINS (ref. #17A030, #18A026, #19A021, #20A014, and #21A039).

412

413 **MDCK cysts**

414 PiggyBac transgenic MDCK cells which constitutively express H2B-EGFP were
415 constructed as follows. To obtain a DNA fragment bearing H2B-EGFP, pcDNA3-H2B-

416 EGFP (Abe et al., 2011) was digested with *HindIII*, blunted, and then digested with *NotI*.
417 pEBMulti-Puro (Wako, Japan) was digested with *BamHI*, blunted, and then digested with
418 *NotI*. Then, the DNA fragment bearing H2B-EGFP was inserted into the pEBMulti-Puro
419 backbone. From this plasmid, a DNA fragment harboring H2B-EGFP was excised again
420 by *XhoI* and *NotI* digestions, and was then inserted between the *XhoI* and *NotI* sites of
421 pPB-CAG-BstXI-IP (a gift from Dr. Hitoshi Niwa)(Nakatake et al., 2013). The resultant
422 plasmid, pPB-CAG-IP-H2B-EGFP, and the PBase-expressing vector pCAGPBase (Guo
423 et al., 2009) were co-transfected into MDCK cells using Lipofectamine LTX (Invitrogen),
424 and the transformants were selected in the presence of puromycin (1 μg/mL). The
425 transformants were expected to express H2B-EGFP under control of the constitutive CAG
426 promoter.

427 To generate and culture cysts of MDCK cells harboring H2B-EGFP, MDCK-
428 conditioned DMEM (Dulbecco's Modified Eagle's Medium containing 10% fetal bovine
429 serum with $NaHCO_3$, Sigma) was used. The conditioned medium was obtained as
430 follows: MDCK cells were cultured in 10 mL DMEM on a 95-mm dish for 4 days at 37°C
431 to reach ~90% confluence, 10 mL fresh DMEM was added, and the cells were cultured
432 for an additional day. The supernatant was obtained, and filtered through a 0.22-μm
433 Millipore filter (Millex-GV SLGV033RS, Millipore, USA), yielding conditioned

434 medium.

435 The cysts were generated and cultured as follows: MDCK cell suspension in 80%
436 MDCK-conditioned DMEM and 20% DMEM was placed on glass-bottom dishes coated
437 with 0.4% agarose (SeaKem GTG agarose, BMA). The cells were cultured for 4–5 days
438 at 37°C, and then subjected to microscopic imaging. Four distinct cysts were analyzed.

439 MDCK cells were described previously (Otani et al., 2019), and were originally
440 provided from Masayuki Murata (University of Tokyo). The identity of the cell line
441 (derivation from canine) was confirmed by genomic sequencing of targeted loci. The
442 mycoplasma was removed, and the removal was confirmed by Minerva biolabs Venor
443 GeM OneStep Mycoplasma detection Kit for Conventional PCR.

444

445 **Microscopic live imaging**

446 Fluorescence images were acquired on a Nikon A1 laser scanning confocal
447 microscope (Nikon, Japan) equipped with a 20× objective (PlanApo; Dry; NA=0.75,
448 Nikon, Japan). A stage-top CO_2 incubation system was used (INUG2-TIZ, Tokai Hit,
449 Japan) on the inverted microscope. H2B-EGFP was excited using a 488-nm laser.

450 For imaging of mouse embryos, 50-100 frames were acquired at 3-min intervals in
451 30–40 z-slices separated by 2.5 μm. For imaging of MDCK cysts, 50-100 frames were

452 acquired at 10-min intervals in 20–30 z-slices separated by 2.0 μm.

453 The confocal images obtained from the mouse embryos and MDCK cells were
454 subjected to the procedure for nuclear detection and tracking. Using the Imaris software
455 (Oxford instruments/Bitplane, UK), the nuclei were automatically detected, followed by
456 manual corrections. The nuclear tracking was also performed automatically followed by
457 manual corrections. Through the manual corrections, the accuracies of the nuclear
458 detection and tracking became essentially 100%, to the best of our judgment.

459

460 **Inference method and simulation procedures**

461 The inference method is as we previously reported (Koyama et al., 2023). Simulation
462 procedures are also as previously reported (Koyama et al., 2023), except that cavities are
463 considered. Details of the modeling of the cavities are described in Supplementary
464 information.

465

466 Acknowledgement

467 We thank Drs. Hitoshi Niwa and Yayoi Toyooka for providing the piggy-bac plasmids
468 and technical suggestions. This work was supported by following grants: Japan Ministry
469 of Education, Culture, Sports, Science and Technology Grant-in-Aid for Scientific

Research on Innovative Areas “Cross-talk between moving cells and microenvironment as a basis of emerging order” for H.K., the National Institutes of Natural Sciences (NINS) program for cross-disciplinary science study for H.K., a Japan Society for the Promotion of Science (JSPS) Grant-in-Aid for Young Scientists (B) for H.K. (17K15131), for Scientific Research (C) for T.O. (18K06234), and for Young Scientists (B) for T.O. (16K18544), a MEXT/JSPS Grant-in-Aid for Scientific Research on Innovative Areas for T.O. (17H05627), the Inamori Foundation for T.O., and the Takeda Science Foundation for T.O.

References

Abe, T., Kiyonari, H., Shioi, G., Inoue, K.I., Nakao, K., Aizawa, S., Fujimori, T., 2011. Establishment of conditional reporter mouse lines at ROSA26 locus for live cell imaging. Genesis 49, 579–590. https://doi.org/10.1002/dvg.20753

Bazellières, E., Conte, V., Elosegui-artola, A., Serra-picamal, X., Bintanel-morcillo, M., Roca-cusachs, P., Muñoz, J.J., Sales-pardo, M., Guimerà, R., Trepat, X., 2015. Control of cell–cell forces and collective cell dynamics by the intercellular adhesome. Nat. Cell Biol. 17, 409–420. https://doi.org/10.1038/ncb3135

Belmonte, J.M., Clendenon, S.G., Oliveira, G.M., Swat, M.H., Greene, E. V., Jeyaraman, S., Glazier, J.A., Bacallao, R.L., 2016. Virtual-tissue computer simulations define the roles of cell adhesion and proliferation in the onset of kidney cystic disease. Mol. Biol. Cell 27, 3673–3685. https://doi.org/10.1091/mbc.e16-01-0059

Brodland, G.W., Conte, V., Cranston, P.G., Veldhuis, J., Narasimhan, S., Hutson, M.S., Jacinto, A., Ulrich, F., Baum, B., Miodownik, M., 2010. Video force microscopy reveals the mechanics of ventral furrow invagination in Drosophila. Proc. Natl. Acad. Sci. U. S. A. 107, 22111–22116. https://doi.org/10.1073/pnas.1006591107

Camley, B.A., Zhang, Y., Zhao, Y., Li, B., Ben-Jacob, E., Levine, H., Rappel, W.J., 2014. Polarity mechanisms such as contact inhibition of locomotion regulate persistent rotational motion of mammalian cells on micropatterns. Proc. Natl. Acad. Sci. U. S. A. 111, 14770–14775. https://doi.org/10.1073/pnas.1414498111

Drasdo, D., Kree, R., McCaskill, J.S., 1995. Monte Carlo approach to tissue-cell populations. Phys. Rev. E 52, 6635–6657.

Dumortier, J.G., Verge-Serandour, M. Le, Tortorelli, A.F., Mielke, A., Plater, L. de, Turlier, H., Maître, J.-L., 2019. Hydraulic fracturing and active coarsening position the lumen of the mouse blastocyst. Science (80-.). 365, 465–468.

Eiraku, M., Takata, N., Ishibashi, H., Kawada, M., Sakakura, E., Okuda, S., Sekiguchi, K., Adachi, T., Sasai, Y., 2011. Self-organizing optic-cup morphogenesis in three-dimensional culture. Nature 472, 51–6. https://doi.org/10.1038/nature09941

Fletcher, A.G., Osterfield, M., Baker, R.E., Shvartsman, S.Y., 2014. Vertex models of epithelial morphogenesis. Biophys. J. 106, 2291–2304. https://doi.org/10.1016/j.bpj.2013.11.4498

Forgacs, G., Newman, S.A., 2005. Biological Physics of the Developing Embryo. Cambridge University Press.

Guillot, C., Lecuit, T., 2013. Mechanics of epithelial tissue homeostasis and morphogenesis. Science (80-.). 340, 1185–9. https://doi.org/10.1126/science.1235249

Guo, G., Yang, J., Nichols, J., Hall, J.S., Eyres, I., Mansfield, W., Smith, A., 2009. Klf4 reverts developmentally programmed restriction of ground state pluripotency. Development 136, 1063–1069. https://doi.org/10.1242/dev.030957

Honda, H., Motosugi, N., Nagai, T., Tanemura, M., Hiiragi, T., 2008a. Computer simulation of emerging asymmetry in the mouse blastocyst. Development 135, 1407–1414. https://doi.org/10.1242/dev.014555

Honda, H., Nagai, T., Tanemura, M., 2008b. Two different mechanisms of planar cell

intercalation leading to tissue elongation. Dev. Dyn. 237, 1826–1836. https://doi.org/10.1002/dvdy.21609

Ishihara, S., Sugimura, K., 2012. Bayesian inference of force dynamics during morphogenesis. J. Theor. Biol. 313, 201–211. https://doi.org/10.1016/j.jtbi.2012.08.017

Israelachvili, J.N., 2011. Intermolecular and Surface Forces, 3rd ed. ed. Elsevier Inc.

Kawagishi, R., Tahara, M., Sawada, K., Morishige, K., Sakata, M., Tasaka, K., Murata, Y., 2004. Na+/H+ exchanger-3 is involved in mouse blastocyst formation. J. Exp. Zool. Part A Comp. Exp. Biol. 301, 767–775. https://doi.org/10.1002/jez.a.90

Kondo, Y., Aoki, K., Ishii, S., 2018. Inverse tissue mechanics of cell monolayer expansion. PLoS Comput. Biol. 1–15.

Koyama, H., Okumura, H., Ito, A.M., Nakamura, K., Otani, T., Kato, K., Fujimori, T., 2023. Effective mechanical potential of cell–cell interaction explains three-dimensional morphologies during early embryogenesis. PLoS Comput. Biol. 19, e1011306. https://doi.org/10.1371/journal.pcbi.1011306

Koyama, H., Shi, D., Suzuki, M., Ueno, N., Uemura, T., Fujimori, T., 2016. Mechanical Regulation of Three-Dimensional Epithelial Fold Pattern Formation in the Mouse Oviduct. Biophys. J. 111, 650–665. https://doi.org/10.1016/j.bpj.2016.06.032

Koyama, H., Umeda, T., Nakamura, K., Higuchi, T., Kimura, A., 2012. A high-resolution shape fitting and simulation demonstrated equatorial cell surface softening during cytokinesis and its promotive role in cytokinesis. PLoS One 7, e31607. https://doi.org/10.1371/journal.pone.0031607

Kurotaki, Y., Hatta, K., Nakao, K., Nabeshima, Y.-I., Fujimori, T., 2007. Blastocyst Axis Is Specified Independently of Early Cell Lineage But Aligns with the ZP Shape. Science 316, 719–23. https://doi.org/10.1126/science.1138591

Maître, J.-L., Berthoumieux, H., Krens, S.F.G., Salbreux, G., Jülicher, F., Paluch, E., Heisenberg, C.P., 2012. Adhesion Functions in Cell Sorting by Mechanically Coupling the Cortices of Adhering Cells. Science (80-.). 338, 253–256. https://doi.org/10.1126/science.1225399

Merkel, M., Manning, M.L., 2017. Using cell deformation and motion to predict forces and collective behavior in morphogenesis. Semin. Cell Dev. Biol. 67, 161–169. https://doi.org/10.1016/j.semcdb.2016.07.029

Miyoshi, H., Satoh, S.K., Yamada, E., Hamaguchi, Y., 2006. Temporal change in local forces and total force all over the surface of the sea urchin egg during cytokinesis. Cell Motil. Cytoskeleton 63, 208–221. https://doi.org/10.1002/cm.20118

Montesano, R., Schaller, G., Orci, L., 1991. Induction of epithelial tubular

morphogenesis in vitro by fibroblast-derived soluble factors. Cell 66, 697–711.

Moriwaki, K., Tsukita, S., Furuse, M., 2007. Tight junctions containing claudin 4 and 6 are essential for blastocyst formation in preimplantation mouse embryos. Dev Biol 312, 509–22.

Nakatake, Y., Fujii, S., Masui, S., Sugimoto, T., Torikai-Nishikawa, S., Adachi, K., Niwa, H., 2013. Kinetics of drug selection systems in mouse embryonic stem cells. BMC Biotechnol. 13.

Nonomura, M., 2012. Study on multicellular systems using a phase field model. PLoS One 7, 1–9. https://doi.org/10.1371/journal.pone.0033501

Otani, T., Nguyen, T.P., Tokuda, S., Sugihara, K., Sugawara, T., Furuse, K., Miura, T., Ebnet, K., Furuse, M., 2019. Claudins and JAM-A coordinately regulate tight junction formation and epithelial polarity. J. Cell Biol. https://doi.org/10.1083/jcb.201812157

Pettitt, B.M., Rossky, P.J., 1986. Alkali halides in water: Ion–solvent correlations and ion–ion potentials of mean force at infinite dilution. J. Chem. Phys. 84, 5836–5844. https://doi.org/10.1063/1.449894

Rivron, N.C., Frias-Aldeguer, J., Vrij, E.J., Boisset, J.C., Korving, J., Vivié, J., Truckenmüller, R.K., Van Oudenaarden, A., Van Blitterswijk, C.A., Geijsen, N.,

2018. Blastocyst-like structures generated solely from stem cells. Nature 557, 106–111. https://doi.org/10.1038/s41586-018-0051-0

Serra, D., Mayr, U., Boni, A., Lukonin, I., Rempfler, M., Meylan, L.C., Stadler, M.B., Strnad, P., Papasaikas, P., Vischi, D., Waldt, A., Roma, G., Liberali, P., 2019. Self-organization and symmetry breaking in intestinal organoid development. Nature 569, 66–72.

Solnica-krezel, L., Sepich, D.S., 2012. Gastrulation: Making and Shaping Germ Layers. Annu. Rev. Cell Dev. Biol. 28, 687–717. https://doi.org/10.1146/annurev-cellbio-092910-154043

Steinberg, M.S., 2007. Differential adhesion in morphogenesis : a modern view. Curr. Opin. Genet. Dev. 17, 1281–286. https://doi.org/10.1016/j.gde.2007.05.002

Style, R.W., Boltyanskiy, R., German, G.K., Hyland, C., Macminn, C.W., Mertz, A.F., Wilen, L.A., Xu, Y., Dufresne, E.R., 2014. Traction force microscopy in physics and biology. Soft Matter 10, 4047–4055. https://doi.org/10.1039/c4sm00264d

Tambe, D.T., Hardin, C.C., Angelini, T.E., Rajendran, K., Park, C.Y., Serra-Picamal, X., Zhou, E.H., Zaman, M.H., Butler, J.P., Weitz, D.A., Fredberg, J.J., Trepat, X., 2011. Collective cell guidance by cooperative intercellular forces. Nat. Mater. 10, 469–75. https://doi.org/10.1038/nmat3025

Wang, A.Z., Ojakian, G.K., Nelson, W.J., 1990. Steps in the morphogenesis of a polarized epithelium. J. Cell Sci. 95, 137–152.

Wang, X., Zhang, Z., Tao, H., Liu, J., Hopyan, S., Sun, Y., 2018. Characterizing Inner Pressure and Stiffness of Trophoblast and Inner Cell Mass of Blastocysts. Biophys. J. 115, 2443–2450. https://doi.org/10.1016/j.bpj.2018.11.008

Yong, J., Moeller, J., Hart, K.C., Ramallo, D., Vogel, V., Dunn, A.R., Nelson, W.J., Pruitt, B.L., 2015. Spatial distribution of cell–cell and cell–ECM adhesions regulates force balance while maintaining E-cadherin molecular tension in cell pairs. Mol. Biol. Cell 26, 2456–2465. https://doi.org/10.1091/mbc.E14-12-1618

610 Figures

611

612 Figure 1: Overview of strategy for inferring the effective potential of cell–cell interactions

613 A. Microscopic forces contributing to cell–cell interactions are exemplified.

614 B. The microscopic forces are approximated as attractive/repulsive forces where cells are

615 described as particles with the mean size.

616 C. Both the repulsive and attractive forces are provided as cell–cell distance-dependent

617 functions, and the summation (black broken line) is the distance–force curve of the two

618 particles. The relationship between the curve and the mean diameters of the cells is shown.

619 D. A cavity-harboring tissue is illustrated with liquid flux into the cavity.

620

621

622 Figure 2: Influence of external constraints to effective forces of cell–cell interaction

623 Simulations were performed on the basis of a distance–force (DF) curve obtained from

624 the Lenard-Jones potential (LJ).

625 A. Expanding cavities are assumed in the particle model. i) An example of simulations

626 with the change in the radius of the cavity. The particles are of the mean size of cells. ii)

627 Inferred effective DF curves with the distant energy barriers (DEBs). The pregiven DF

628 curve (LJ) is shown in a broken black line. The numbers of the particles are the same

629 among the different cavities.

630 B. Expanding cavities are assumed whereas cell–cell interaction forces are not introduced.

631 i) An example of simulations. ii) Inferred effective DF curves.

632 C. Reconstruction of cell–cell interaction forces under expanding cavities. i) All the data

633 points in A and B under the radius of the cavity = 9.7 -> 14.2μm are plotted on distance–

634 force graph as a heat map, and the binned averages were calculated (yellow) which

635 correspond to the DF curves in A and B. ii) DF curves obtained by subtracting the DF

636 curves in B from those in A: i.e., A – B as exemplified in C-i. The definition of the heat

637 map is described in Supplementary information

638 D. The subtraction performed in C is schematically explained in the relationship among

639 A, B, and C. See the main text.

640 Related figure: Figure S1 (simulation procedures and inferred DF curves under non-

641 expanding cavities).

642 Related movie: Movie S1 (simulation)

643

644

645 Figure 3: Inference of the effective force of cell–cell interaction in mouse blastocysts

646 A. Blastocyst stages of mouse embryo are illustrated, and their confocal microscopic

647 images are shown: bright field, maximum intensity projection (MIP) and cross-section of
648 fluorescence of H2B-EGFP. Snapshots of nuclear tracking are also shown; blue spheres
649 indicate the detected nuclei. ICM cells are located around the bottom region of the image,
650 as indicated by *. Scale bars = 15μm.
651 B. Inferred effective DF curve in the mouse blastocyst (ref line). DEB is indicated. For
652 comparison, an inferred effective DF curve from the compaction stage embryo before
653 forming cavities is shown which we previously reported (green line) (ref).
654 C. Inferred effective DP curves in the mouse blastocysts. Four embryos were examined.
655 An enlarged view around longer distance is also shown in the inset.
656 D. Inferred effective DP curves in the mouse embryos where the cavitation was inhibited.
657 S3226 whose target is Na+/H+ exchanger inhibits the cavitation of the blastocyst
658 (Kawagishi et al., 2004). In the left panel, the microscopic images are shown. In the right
659 panel, the DF curves from three embryos are shown.
660 Related figure: Figure S2 (experimental procedures of S3226 treatment)
661
662
663 Figure 4: Inference of effective force of cell–cell interaction in cysts formed by MDCK
664 cells

665 A. MDCK cysts formed under suspension conditions are illustrated, and confocal
666 microscopic images are shown: bright field, maximum intensity projection (MIP) and
667 cross-section of fluorescence of H2B-EGFP. Scale bars = 10μm.
668 B and C. Inferred effective DF and DP curves. In C, an enlarged view is also provided. A
669 DEB is indicated.
670 Related figures: Figure S3 (DP curves from other cysts).
671
672
673 Figure 5: Outcomes of simulations based on inferred distance–force curves with DEBs
674 A. Initial configurations of particles are exemplified, that harbor a cavity. A cross-section
675 is also shown in the right panel.
676 B-E. Simulations results under the effective DF curves derived from the mouse blastocyst
677 (B), and the MDCK cyst (C), and the synthetic tissue harboring an expanding cavity (D)
678 in Fig. 2 are shown. E is the simulation result under the LJ potential for comparison. In
679 addition to the left panels ("Full DF curves"), the DF curves in which the DEBs were
680 artificially eliminated were used in the right panel ("DF curves w/o DEB); in D and E,
681 analyzes for the right panel were not performed ("ND"). For each simulation result, cross-
682 sections are also shown, and in the case of the mouse blastocyst, two parallel cross-

683 sections (shown in blue and green) are merged.

684

685

686 Figure 6: Modeling of distance–force curves and diagrams of simulation outcomes;

687 cavity-harboring structures

688 A. Modeling of DF curves using four parameters: N, D_0, δ, and ε. In the left panel, a DF

689 curve without the cosine term is always >0 (repulsive) ($F = \varepsilon D^{-N}$, green broken line).

690 Upon introduction of the cosine (purple broken line), the curves acquire regions with <0

691 (attractive) and a DEB (red line). Upon introduction of D_0, the curves are translated along

692 the distance (blue line). As shown in the blue line, the DEB ranges from $3\delta/4+D_0$ to

693 $5\delta/4+D_0$ (D_2). In the right panel, N affects the gradient of the curves and the height of

694 DEBs, and thus, the relative strength of DEB is modified.

695 B. Outcomes of simulations under various values of N and D^* in the presence of DEB.

696 From the equation defined in A, DF curves from $D = 0$ to D at the end of DEBs (w/ DEB)

697 were used as exemplified in the graph of DF curve ("w/ DEB"). The initial configuration

698 is shown in the left bottom. On the diagram, some conditions were designated by symbols

699 (circle, square, and triangle), and their simulation results are visualized on the bottom row

700 (blue spheres) with the profiles of the DF curves. Cross-sections are visualized for some

simulation results. The diameters of the blue spheres are equivalent to the mean diameter. For "cup" [orange rings, mouth of the cup; white dots, particles located on the ring; crosses, the particles located neither on the ring nor at the center of the ring]. For "tube" [orange crosses, open ends of the tube]. For "cavity with extra particles" [arrows, extra particles where multiple- but not single-layered]. D_1, mean diameter; D_2, distance of DEBs. The definition of each phase is explained in Supplementary information. Gray crosses, data points of all simulations for depicting the lines separating each phase.

C. Simulation outcomes in the absence of DEBs. DF curves from $D = 0$ to D before starting DEB (w/o DEB) were used as exemplified in the graph of DF curve ("w/o DEB").

Related figure: Figure S4 (phase diagrams under a different number of particles), S5 (maintenance of tubes was examined under DF curves with DEBs).

Related movie: Movie S2 (the cavity-harboring structure was stably maintained under fluctuations)

Figure 7: Diagrams of simulation outcomes; 2D sheets, spherical/non-spherical aggregates

A. Outcomes of simulations starting from a two-dimensional (2D) sheet with slight

positional fluctuations. The results are shown in a similar manner to Fig. 6B, except that the diameters of the blue spheres are equivalent to 0.4× the mean diameter. D_1, mean diameter; W_1, width of attractive force regions; P_1, potential energy derived from attractive forces.

B. Simulation outcomes without DEBs.

Related figure: Figure S6 (possible morphological transitions)

Related movie: Movie S2 (2D sheets were stably maintained under fluctuations), and Movie S3 (possible morphological transitions).

Figure 8: Radial distribution functions (RDF) in 2D and 3D situations

A. Comparison of inferred DF curves in 2D (i) and 3D (ii) situations. The DF curves are shown with snapshots of simulations and with the pregiven potentials (LJ). DEB is indicated. The condition of the simulations is [sampling interval = 3 min, SD value of force fluctuation = 1000%, and persistency of force fluctuation = 1 min].

B. The relationship between RDF and effective pairwise potentials is described. An RDF for the central particle (dark blue) is illustrated. Densities of particles are shown as the function of distances from the central particle. Higher density at a distance means an

energetically favorable state, and therefore, the potential is expected to be lower at the distance.

C. RDFs in 2D and 3D situations were calculated in simulations under the LJ potential. The snapshots of the simulations and the RDFs are shown. In these simulations, fluctuations of the forces given by the LJ potential were introduced with the persistency. Under longer persistency, the particles tend to easily change their positions. The condition is [SD value of force fluctuation = 300%, and persistency of force fluctuation = 1 min].

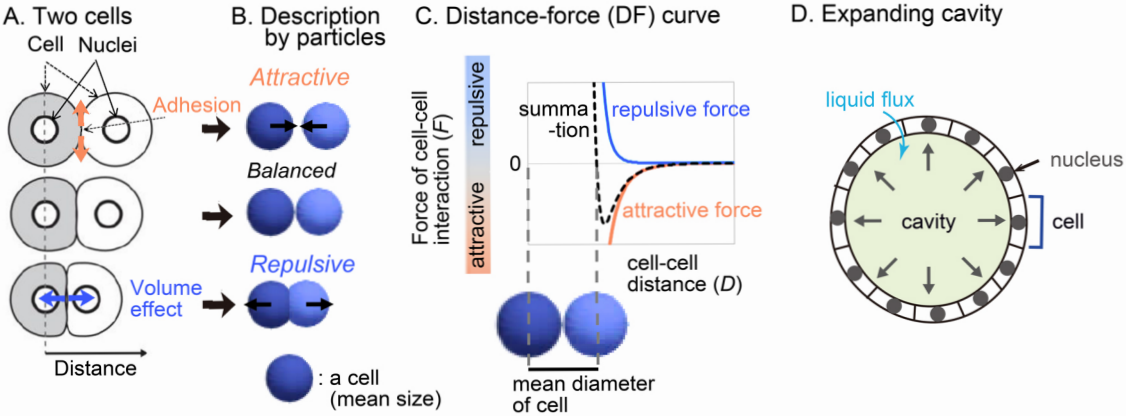

Fig.1 Koyama et al.

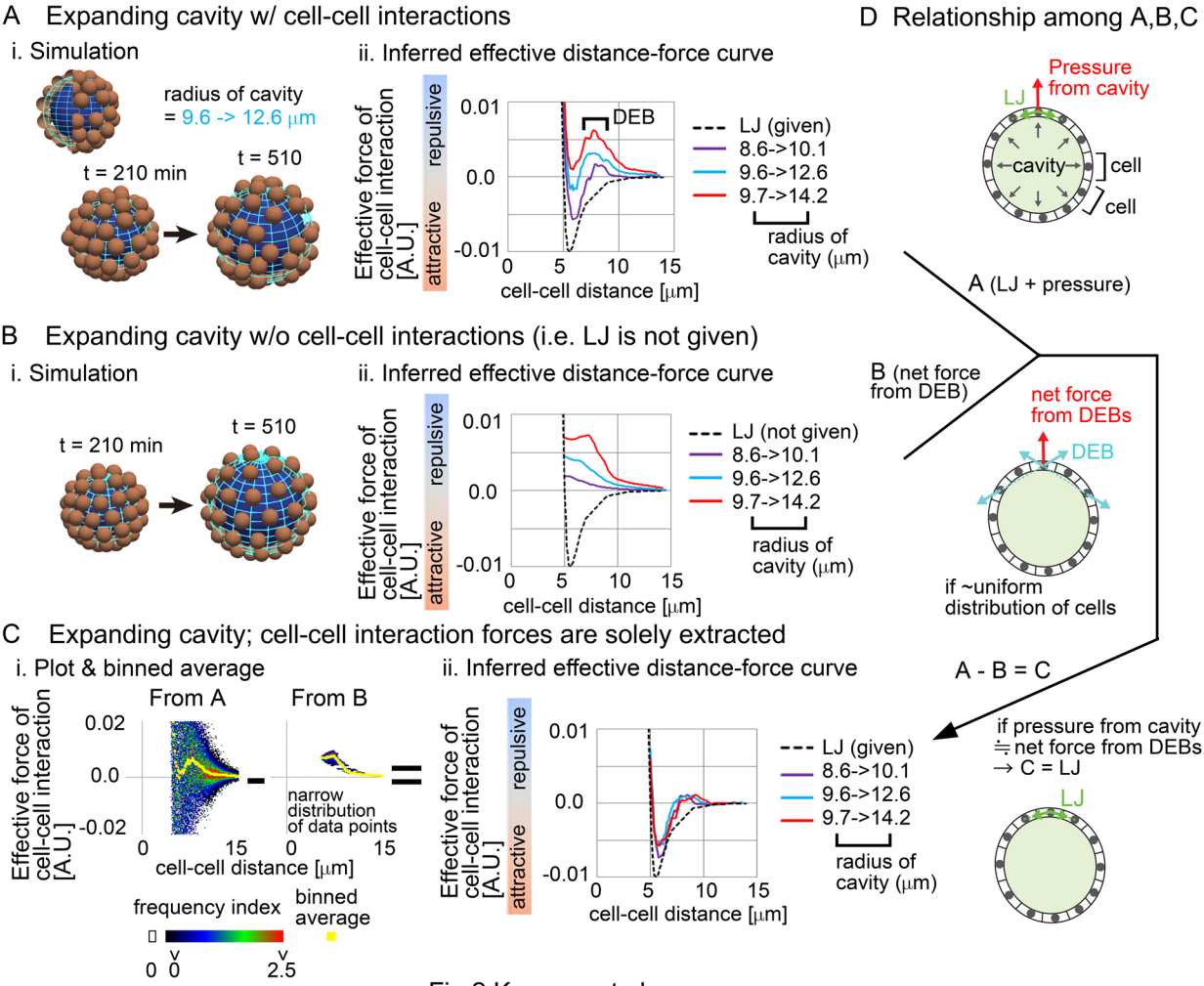

Fig.2 Koyama et al.

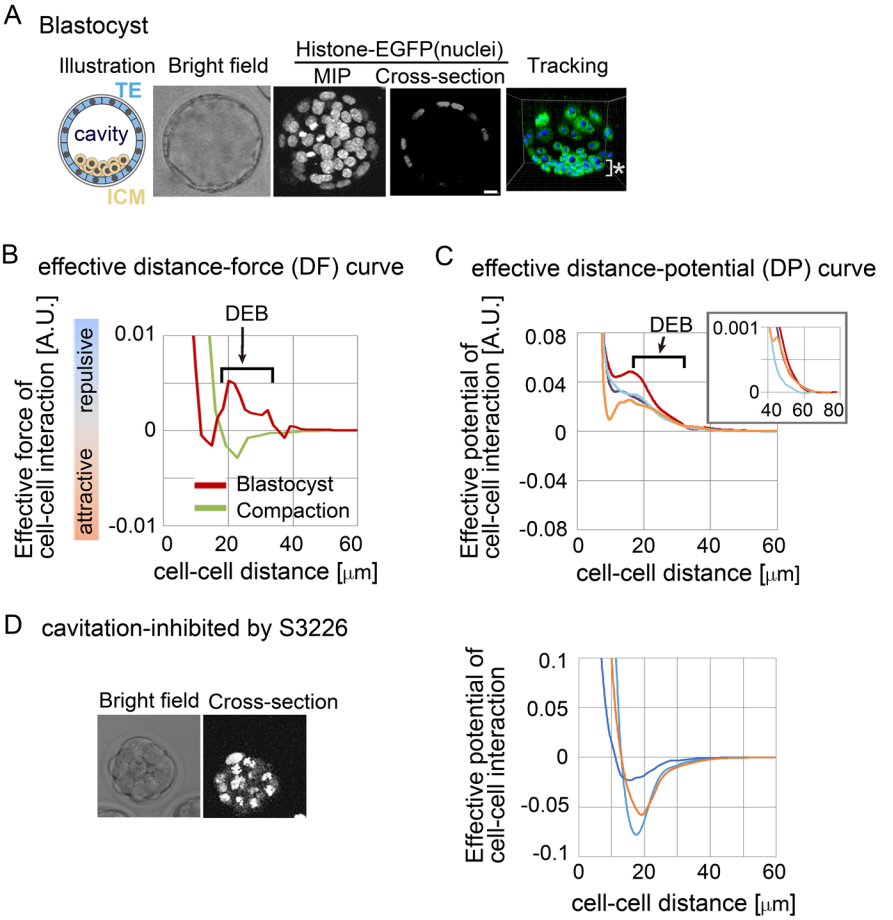

Fig. 3 Koyama et al.

A

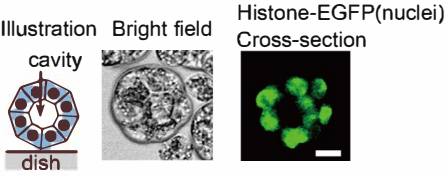

B

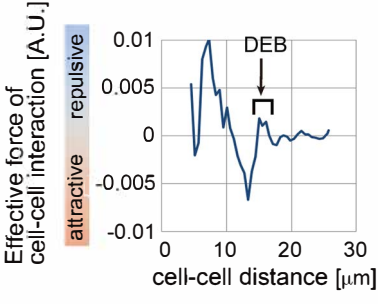

C

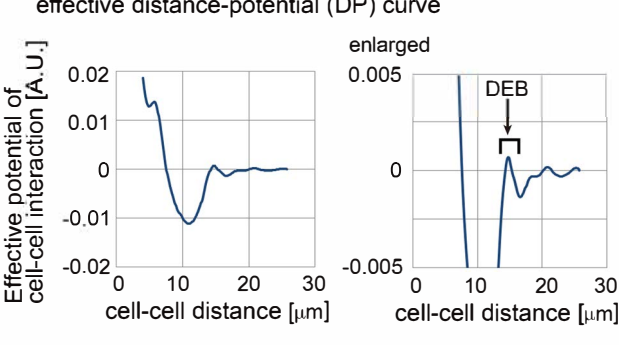

Fig.4 Koyama et al.

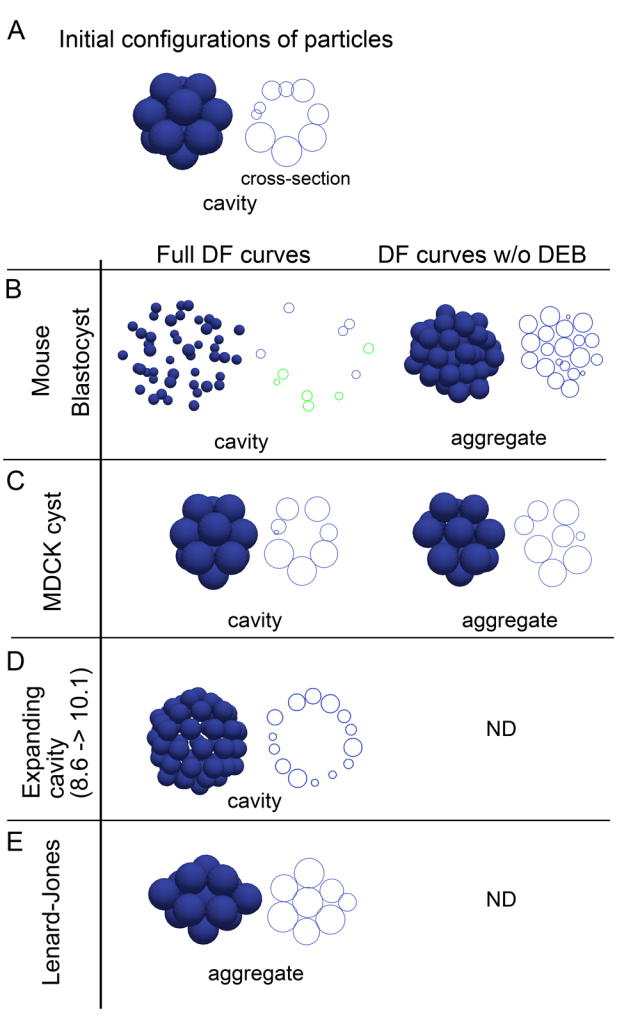

Fig.5 Koyama et al.

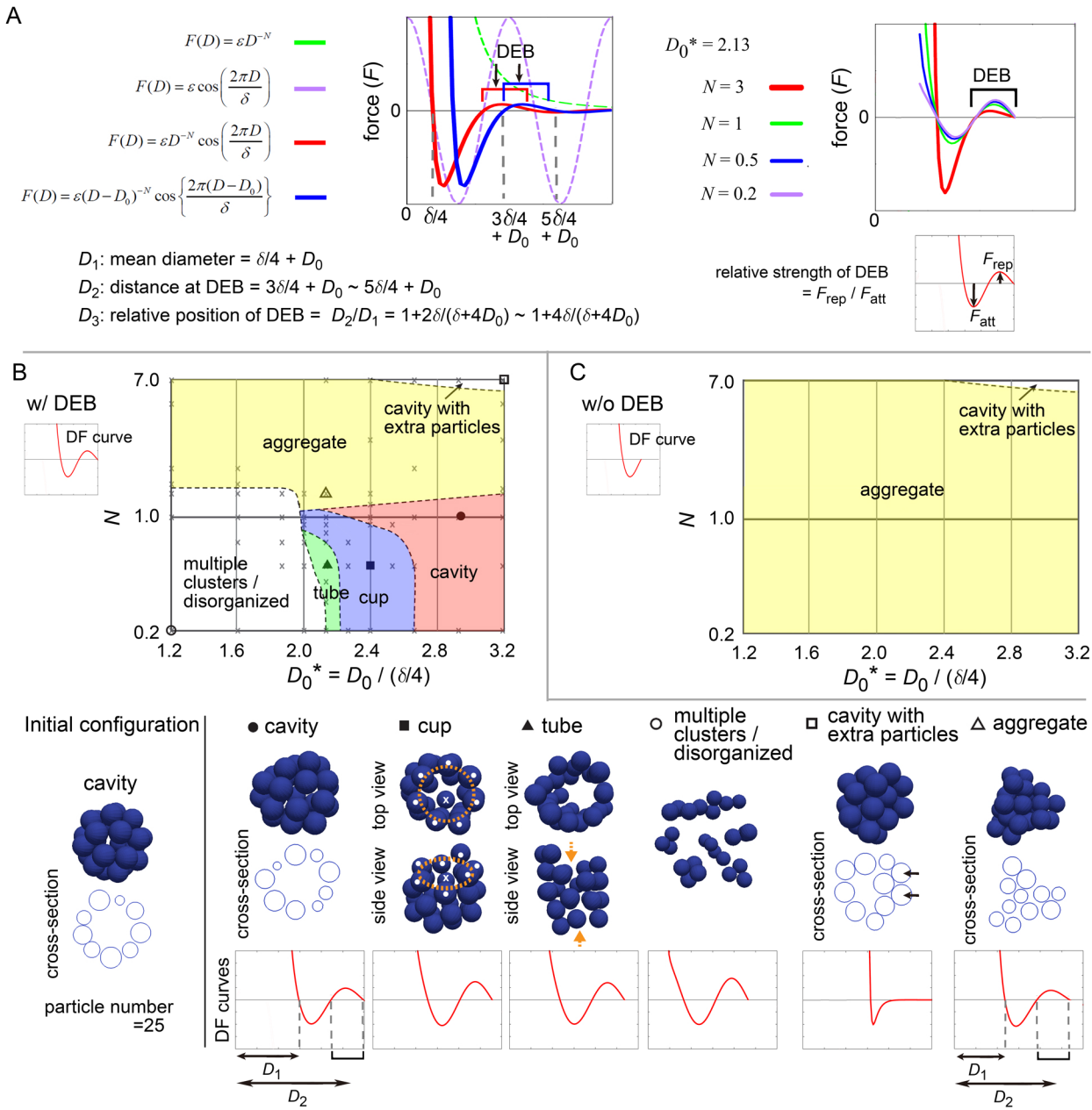

Fig.6 Koyama et al.

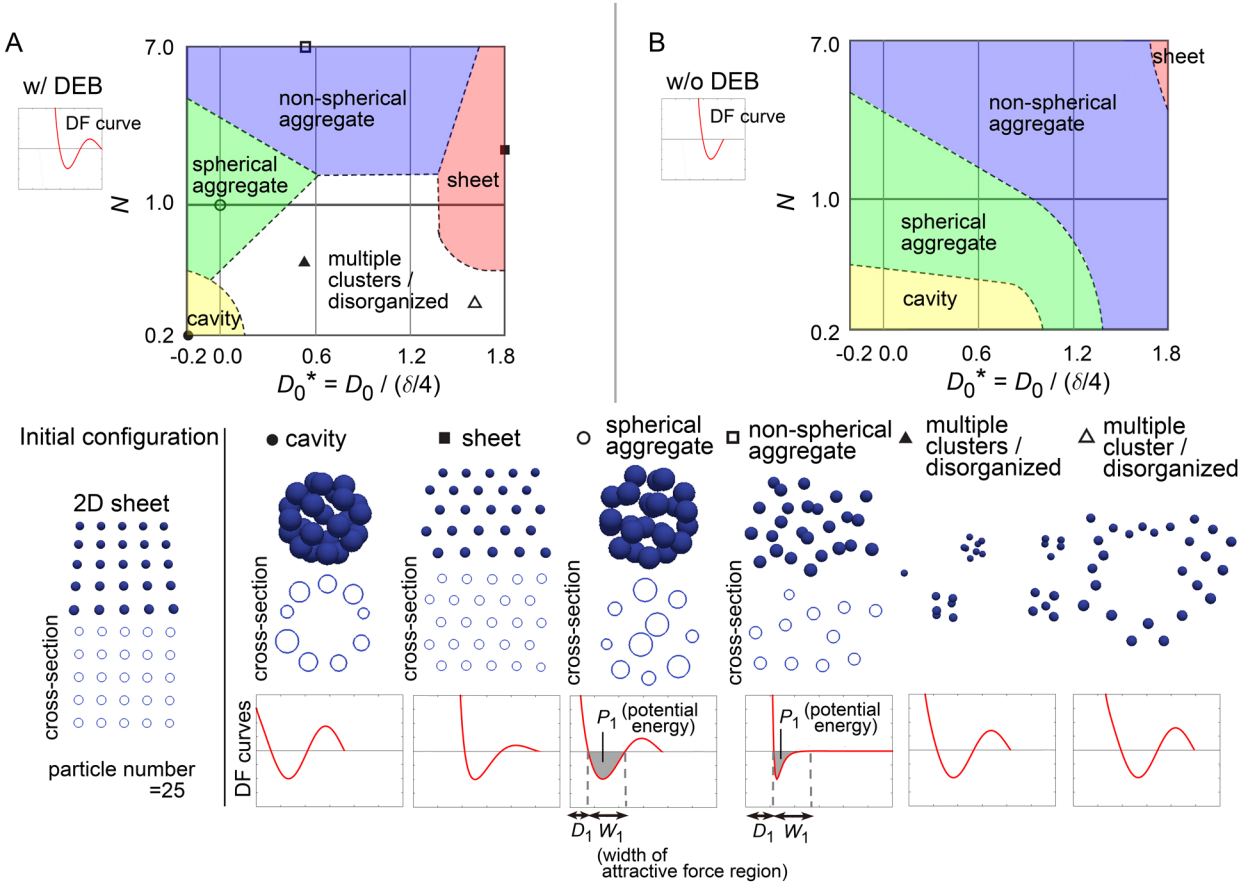

Fig.7 Koyama et al.

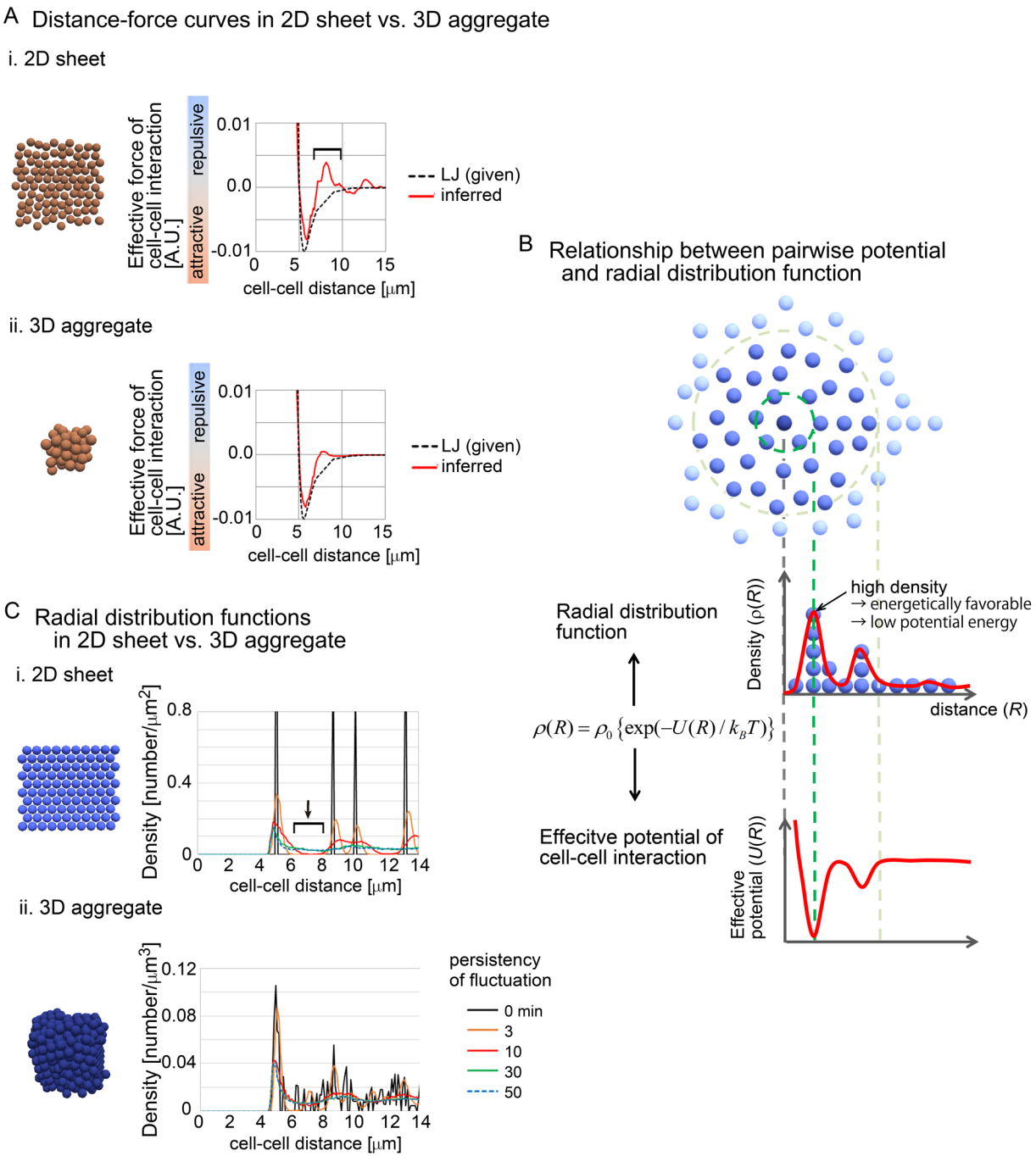

Fig.8 Koyama et al.